

Fabrication of microparabolic reflector for infrared antenna coupled detectors

Mohamed H. Mubarak¹ ✉, Othman Sidek¹, Mohamed R. Abdel-Rahman², Mohamed Tafir Mustaffa¹, Ahmed Shukri Mustapa Kamal³, Saad M. Mukras⁴

¹School of Electrical and Electronic Engineering, Universiti Sains Malaysia, 14300, Pulau Pinang, Malaysia

²Electrical Engineering Department, King Saud University, Riyadh, Saudi Arabia

³School of Physics, Universiti Sains Malaysia, 11800, Pulau Pinang, Malaysia

⁴Mechanical Engineering Department, Qassim University, Buraydah, Saudi Arabia

✉ E-mail: moh.habashy@gmail.com

Published in Micro & Nano Letters; Received on 30th November 2017; Revised on 19th April 2018; Accepted on 8th June 2018

The fabrication process of a microparabolic reflector using isotropic xenon difluoride (XeF_2) etching technique is presented and analysed through this work for developing infrared antenna-coupled detectors. Although many parametric studies described the behaviour of this process in the literature, the non-linearity of the process and its dramatic dependency on the pattern definition result in great difficulties when adopting the process for developing a particular structure. The main focus of this work is, therefore, to present a detailed etching analysis as dictated in the proposed design providing the proper etching recipe according to the proposed structure design and its associated masking pattern. Deep insights into the process have been highlighted suggesting the necessity of the process assessment in terms of evaluating the three-dimensional etched volume rather than the etched depth. This will potentially solve the non-linearity behaviour and the pattern dependency problem. The optimum etching recipe yields approximately a total volume of 0.354 mm^3 through the proper patterning mask. The resultant parabolic cavities have 75 and $13 \mu\text{m}$ in their diameter and depth, respectively, as required for the proposed structure. The integration of a microparabolic reflector with such detectors will potentially enhance the specific detectivity of these detectors.

1. Introduction: Nanoantenna coupled infrared (IR) detectors have received a significant interest of many researchers for their high speed uncooled detection with spectral and polarisation selectivity [1, 2]. Since these devices are addressing the wave nature of the light, which is then regarded as a propagating electromagnetic field [3], a nanoantenna had been thus used to harvest the radiation, optimising the energy transfer from the freely propagating radiation field to the localised sub-wavelength sensor [4]. The extremely low detectivity of these detectors, at least about three orders of magnitude compared to the other cryogenic-cooled IR detectors counterparts [5], is the main impediment for these devices from being widely commercialised. Considerable efforts have been made to improve the overall efficiency either by increasing antenna coupling efficiency [2, 6–10], sensing device efficiency [10–12], and impedance matching efficiency between both the antenna and the sensing device [1, 13]. An integrated microparabolic reflector nanoantenna coupled structure was proposed in [14, 15] and is expected to contribute with a considerable increase in the detectivity through the reduction in the substrate modes losses, and an added space diversity gain via the new larger optical active area of the device.

To fabricate such a structure, the micromachining of a parabolic reflector structure via an isotropic etching technique is prescribed. The standard isotropic xenon difluoride (XeF_2) etching is a well-known dry etching mechanism for silicon (Si) micromachining which can be used to develop the complex three-dimensional (3D) microstructures. It is based on a gaseous phase chemical diffusion reaction of the fluorine ions into Si at room temperature to produce the volatile tetrafluorosilane (SiF_4) gas without any need of plasmas or catalysts [16, 17]. This will thus offer a very simple and cost effective solution while maintaining the CMOS compatibility. In addition to SiF_4 , etch products have also been reported to include some trace amount of other different silicon fluoride by-products, which make the reaction kinetics quite puzzling and not fully understandable [18, 19]. This motivated different researchers to study and analyse the reaction kinetics and mechanisms [20–22].

Several parametric studies have previously been presented illustrating the Si etching characteristics and providing an estimate for the etching rate [16, 18, 19, 23–25]. Some efforts have also been placed into modelling and simulating this process [26]. However, this process generally shows a non-linear etching behaviour and is dramatically dependent on the loaded sample conditions as well as the masking pattern [18, 19, 24]. This explains the huge variation of the reported numerical values of the etching results. There is currently no prescription in the literature that can be generalised and great difficulties will be thus encountered while adopting the process for a particular pattern. The etching process was analysed in close vicinity according to the designed pattern for the proposed structure in particular as well as the etching load which is defined as the total surface area subjected to the etchant gas.

This work will thus present a case study that is concerned with adopting the XeF_2 etching process to implement the novel structure of integrated microparabolic reflector nanoantenna coupled detector. The general guidelines to adopt this etching process for a particular structure will be highlighted while estimating the proper size of the masking pattern, the load and the etching recipe. In this Letter, the design of the device will first be introduced providing all details for the feeder antenna element, the bolometer and the reflector with the entire requirements for the reflector integration. The masking pattern and the constraints on the recipe will be defined accordingly. The detailed fabrication process that was followed throughout this work will then be described. The detailed analysis of the cavity micromachining as required for the proposed design will be outlined focusing mainly on the total Si etched volume. Some different conditions that may influence the process will be considered. The final optimum etching recipe to achieve the proposed structure, according to the used pattern, will be reported.

2. Pattern dependency: The XeF_2 etching technique has been extensively studied in the literature [16, 18, 19, 23–27]. The studies reported an average etching rate that varied from 0.46 to

Table 1 Numerical analysis of a hypothetical etching example for studying the influence of masking pattern effect

Pattern shape	Large circular	Small circular	Square
aperture size, μm	40	20	35.5
aperture area, μm^2	1256	314	1256
etched volume, μm^3	84,823	25,132	20,656
varied etched depth, μm	10	20	24

22.5 $\mu\text{m}/\text{min}$. The large variation in the etching rate as measured in the literature is referred back to the differences in the assigned masking pattern for the mentioned studies in terms of the pattern shape, size and density. Moreover, the non-linearity of the etching rate has also been observed where there is a dramatic drop in the rate with the increased number of cycles and even within a single etching cycle.

To overcome the non-linearity as well as the pattern dependency and to provide reputable and linear characteristics for the process, a different assessment methodology is suggested.

To date, all the analysis presented in the literature are concerned mainly with the study and evaluation of the process in terms of the single-dimensional etching depth. However, since this process is an isotropic technique that propagates along 3D, the proper analysis and assessment for this process should be presented in terms of the 3D etched volume of Si. Meanwhile, the etchant gas volume should be monitored to ensure the full dependency on time without any limitation of the etchant gas.

To illustrate the influence of the masking pattern on the etching result, three different patterns are analysed in Table 1 representing a hypothetical etching example. The etching is assumed to propagate equally in both lateral and vertical directions. Both square and large circular patterns are selected to demonstrate the influence of the pattern shape while showing same exposed area. The large and small circular patterns, on the other hand, show the influence of the aperture size that shows, in this case, a drop to a quarter of the large circular pattern area. From the table, it is fairly obvious that if the etching is limited to a depth of 10 μm , the shape of the pattern will result in a great variation in the total etched volume.

Therefore, when the process is time controlled, a deeper etching is highly expected through the square pattern to achieve the same etched volume as that obtained through the circular pattern. For instance, if the process is limited to an etched volume of 84823 μm^3 , the etching through the square pattern can reach to a depth of 24 μm compared to 10 μm for the circular pattern. Similarly, the small circular pattern will show an etching depth increase up to 20 μm . This explains the non-linearity and pattern dependency of the process and suggests that, as long as the process is time controlled, the proper assessment for the process should be presented in terms of the total etched volume.

3. Structure design and pattern definition: The antenna for the new integrated structure of concern here, as illustrated in Fig. 1, is composed mainly of a half wavelength dipole as the feeding antenna element, a parabolic reflector and a cavity filling/standoff dielectric layer. A similar antenna structure has been previously simulated and found to have an expected antenna gain increase of 20 dB [14]. A sub-wavelength bolometer is implemented as a sensing element at the dipole feeding point. The SU8 photoresist is assigned as the standoff layer functioning as the insulating layer and the separating dielectric between the feeder and the reflector. The relative dielectric permittivity of SU8 used in the design of the structure is $2.92 + j6.88 \times 10^{-3}$ at the wavelength of interest as can be estimated from [28].

The new antenna structure is believed to offer a significant reduction in the substrate modes losses due to the air-side illumination

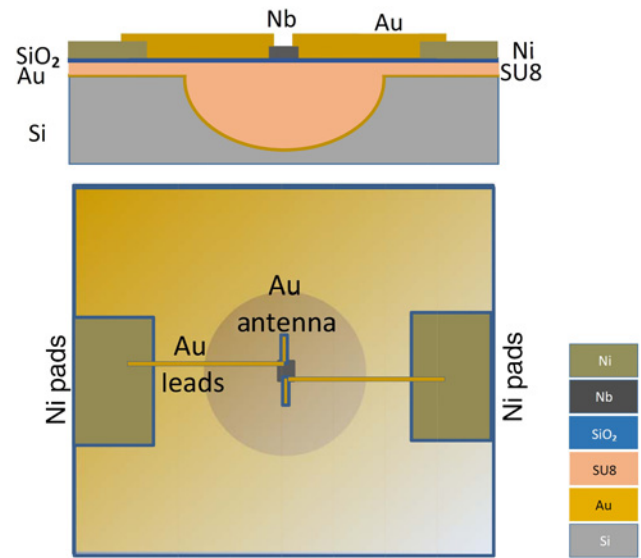


Fig. 1 Parabolic reflector integrated structure illustration: sectional view (up) and top view (bottom)

while confining the trapped waves back to the feeding antenna at the focal point of the cavity reflector. The new larger optical active area of the device, which is represented by the effective aperture of the cavity rather than that of the single dipole antenna, is also conceived theoretically to add a substantial space diversity gain. As a result of the mentioned advantages, a considerable enhancement of the device detectivity is highly expected.

According to the quasi-static model, the effective resonant wavelength, λ_{eff} , can be calculated using

$$\lambda_{\text{eff}} = \frac{\lambda_0}{\sqrt{\epsilon_{\text{eff}}}} \quad (1)$$

where λ_0 is the radiation wavelength in free space, ϵ_{eff} is the effective dielectric constant represented by the average of the dielectric constant of both the air and the substrate due to the air-dielectric interface. Since the SU8 is the standoff layer in this work, then the substrate permittivity $\epsilon_{\text{sub}} = 2.95$ at 10.6 μm . Accordingly, the effective permittivity is then $\epsilon_{\text{eff}} = 1.975$. By substitution into (1), the effective resonant wavelength is determined to be $\lambda_{\text{eff}} = 7.54 \mu\text{m}$. The parabolic reflector is engineered through the design of its diameter as well as the height of its focal point. While the aperture diameter is required to be much greater than the wavelength for the validity of the design model assumptions [29], it is however bounded on the other hand by the pixel size. A reflector aperture of 75 μm in diameter is therefore proposed to yield about ten times greater λ_{eff} while providing a pixel area quite close to the commercially available pixel of 50 $\mu\text{m} \times 50 \mu\text{m}$ that is utilised for IR thermal imagers [30].

The surface profile of the reflector will be totally controlled by the cavity etching process. The height of the reflector focal point, f , can then be assigned according to the cavity surface profile in terms of the cavity aperture diameter, d , and the cavity depth, Z_{cav} by

$$f = \frac{d^2}{16Z_{\text{cav}}} \quad (2)$$

The proper selection of the successfully etched cavities is thus limited to those of the focal height, f , higher than the etched depth such that the continuity of the complete device can be guaranteed.

A masking pattern of circular windows will be used throughout this work. To estimate the size of the masking pattern, it was first

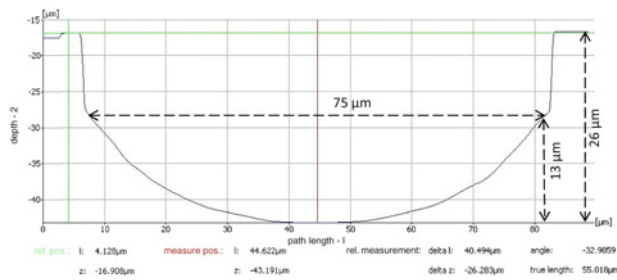


Fig. 2 Cavity profile for one successful sample showing the measurements of d , Z_{cav} and the etching depth

assumed that the etching process will be completely isotropic resulting in cavity structures of a pure spherical profile. Accordingly, this assumption will yield the equality of the focal height and the cavity depth, $f = Z_{cav}$. By substituting in (2), the required cavity depth will then be $Z_{cav} = 18 \mu\text{m}$. This reveals that the circular pattern is required to have a diameter of $39 \mu\text{m}$ in order to achieve a final aperture diameter of $75 \mu\text{m}$.

However, starting with a flat surface profile, the vertical and lateral etching will be trading with each other rendering the flat surface profile to a parabolic one. In contrast to the above assumption, the actual vertical to lateral etching ratio will exceed unity. This will result in a deeper etched structure for the required cavity profile to be attained. The exact etching recipe can be optimised through circular etching patterns of different diameters that vary around the calculated value ranging from 30 to $50 \mu\text{m}$.

Fig. 2 shows the measurements of the etching profile for one example of the successfully etched samples. It is fairly obvious that the height of the reflector focal point, $f = 27 \mu\text{m}$ as calculated for the parabolic cavity of 75 and $13 \mu\text{m}$ in its diameter and depth, respectively, is $1 \mu\text{m}$ higher than the etched depth as required for the implementation considerations.

4. Fabrication technique: In the preparation of the substrate, as illustrated in Fig. 3, the microparabolic reflector is first

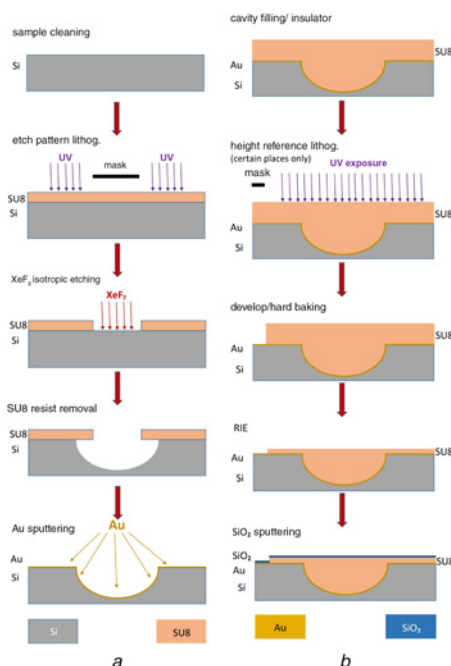


Fig. 3 Substrate preparation process flow
a Cavity etching,
b Cavity filling

constructed in a bulk single crystalline Si substrate. A low resistivity $\langle 100 \rangle$ Si wafer with a thickness of $380 \mu\text{m}$ is thus diced into $1 \text{ cm} \times 1 \text{ cm}$ samples. The micromachining process is carried out using XeF_2 isotropic dry etching process in the XACTIX etching machine.

A circular windows pattern with an average diameter of $38 \mu\text{m}$ is first transferred to the substrate through a photolithography process in a $2.2 \mu\text{m}$ thick SU8 photoresist mask to define the area to be etched as well as the size of the required cavity. Due to the high selectivity of the XeF_2 etching technique, the formed native oxide layer on the substrate as well as any surface contamination can dramatically slow down or even prevent the etching process. So, the samples have to be briefly dipped into hydrofluoric acid 49% (HF) and DI water (1:50 volume ratio) for about 20 s to remove any oxide layers and then dehydrated prior to the etching process. However, throughout this work, the samples cannot be processed immediately after native oxide removal but have to be introduced to the etching process within 24 h later. Moreover, due to the use of the SU8 photoresist for masking, the dehydration step is also limited to 2 min at 95°C to avoid the hard baking of the photoresist whereas a higher temperature of 140°C for 5 min is recommended. Etching process has to be then carried out for only one loaded sample at a time using a few etching cycles, each of 30 s, and with an etchant gas pressure of 3 Torr.

After the etching process, the rough estimation of the etched depth can be measured using the optical microscope while the detailed etching analysis, including the precise measurement of diameter, etching depth and etching profile, can only be conducted after removing the photoresist mask using the 3D microscope as shown in Figs. 2 and 4.

By achieving the required cavity surface profile, the micro-machined cavities are then coated by 10 nm/120 nm Ti/Au layer using the RF sputtering to form the reflector walls. The RF sputtering has been conducted at a process pressure of 1.5×10^{-4} mTorr with 9 sccm Ar gas flow and RF sputtering power of 200 and 50 W for both Ti and Au, respectively. An annealing process is then introduced for 20 min at 250°C to enhance the layer adhesion. The spin coating of the SU8 was then followed at 2000 rpm to form the standoff insulating layer.

The SU8-10, in particular, was found to give the best filling with the maximum flatness. In this regard, the AFM measurement over the aperture of the cavity had shown a maximum height variation of 350 nm. The sample is then subjected to a photolithography process to pattern the sample boards providing the surface of the sample as a height reference level required in the consequent processes.

The SU8 photoresist hard baking is then conducted in a tube furnace at 200°C for 15 min. The reactive ion etching (RIE) is then introduced at a rate of $1.5 \mu\text{m}/\text{min}$ through a typical plasma oxidation recipe using 200 W of RF power at a 50 mTorr

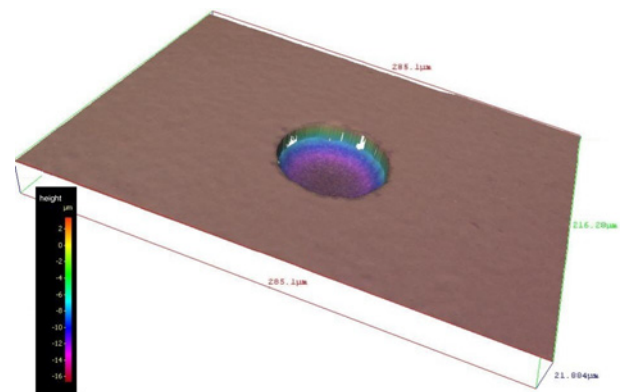


Fig. 4 3D microscope image for a completed etched cavity

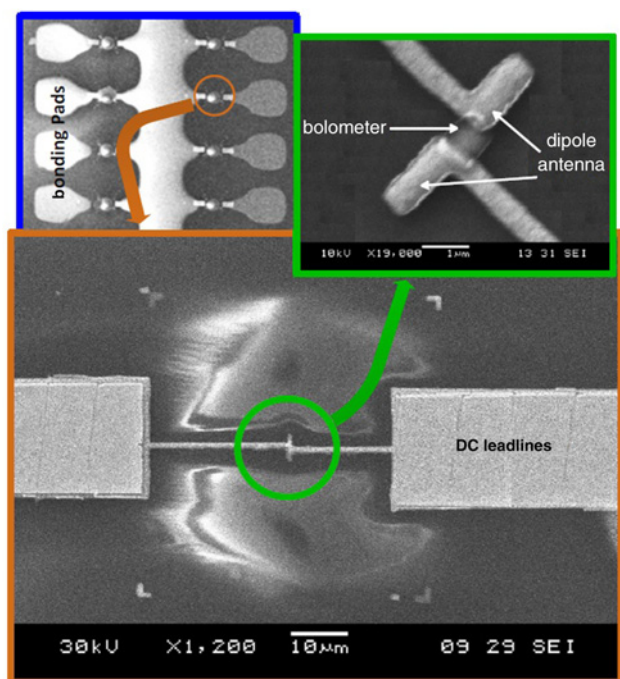


Fig. 5 Scanning electron micrograph of a complete integrated device

chamber pressure in a gas flow of 50 and 5 sccm of both O_2 and CF_4 , respectively. An additional 50 nm layer of SiO_2 is then sputtered to provide more protection to the SU8 filling against any solvent used in the subsequent processes. SiO_2 has been sputtered with a deposition rate of 0.4 Å/s using RF sputtering power of 250 W at a process pressure of 4.6×10^{-4} mTorr with 7 sccm Ar gas flow.

To complete the structure, the bonding pads have to be patterned using photolithography and liftoff process. The bolometer should then be implemented at the focal point of the reflector using the electron beam lithography and liftoff process. In the same manner, the dipole antenna with the leadlines will consequently be patterned. According to the initial attempt for fabricating the device, the parabolic reflector integrated nanoantenna coupled IR detector is completely structured as shown in Fig. 5.

5. Analysis and results: During the fabrication process of the proposed device, the isotropic etching using XeF_2 was studied extensively in close vicinity. Deep insight into etching mechanism revealed that this etching process is primarily limited by the etching time in terms of both the number of cycles and the cycle duration. Furthermore, while analysing the etching behaviour via different sized patterns, it was observed that the process is highly dependent on the pattern shape and dimensions.

The size of the pattern mainly defines the initial etching load from one point of view. The larger patterns will definitely acquire more etchant gas and thus experience a lower etching depth. Moreover, the aspect ratio of the structure influences also the behaviour of the etching as well. Whenever the patterned structure provides a high aspect ratio, the etchant gas molecules will be trapped in the patterned structure's wall increasing the probability of equal vertical and lateral etching. This will, therefore, provide an etching with a more isotropic behaviour tendency. This explains the change of etching profile from a spherical to a flat profile with the increased size of the opened pattern [18].

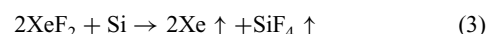
The very low etch rate at the first two cycles of the process is commonly observed for all samples suggesting that the etchant gas is depleted by the native oxide layer, which is in good agreement with the literature [18, 19]. The formation of a tough white

film, which is interpreted as a silicon fluorine polymer [18], had been observed on the surface of some samples indicating the presence of water or moisture. This film explains the deficiency or even the absence of etching rate in some cases with no dehydration baking process. On the other hand, a dark grey colour points out the change of the surface roughness after etching. The surface colour change has been noticed on the top as well as the backside of the sample reveals that the backside contributes to the extra loading effect which is not taken into consideration through this work.

The time dependency has been studied for different combination sets of a number of cycles and cycle duration for tuning the etching recipe. For proper etching analysis, it is necessary to avoid etching saturation. This is done by providing a sufficient volume of the etchant gas during the process. In this study, a constant gas pressure of 3 Torr was thus maintained through multiple etching cycles that had a duration of 30 s each. Moreover, constant etching load must also be maintained between the different experiments and this is achieved by introducing identically patterned samples in the analysis. From a large number of etched samples, only five samples have been selected here to summarise the etching analysis as detailed in Table 2. These samples have been subjected to etching through a circular windows pattern of a 38 μm in diameter initially and with a total patterned area of 3.7122 mm^2 .

A significant preferential vertical depth etching over lateral undercutting, in the range of 20–40%, is measured in most of the etched samples through this work. The approximated value for the etched volume has been calculated and tabulated showing a maximum value of 0.354 mm^3 as calculated for the highest measured sample, S_5 .

As the required volume of the etchant gas increases with time, the maximum amount of etchant gas is best calculated according to the final resultant load. Referring to the data logs captured by the etching machine, the total volume of consumed gas during one etching experiment is 105 and 90 mg for the cases of 5 and 4 etching cycles, respectively, including the pre-etch cycles as well. The gas consumption per etching cycle, excluding the pre-etch cycles, is thus around 15 mg. Given that the molecular mass for the etching gas is 169.29 g/mol, the number of moles can be then found to be 8.86×10^{-5} that is sufficient to etch 4.43×10^{-5} moles of Si according to the following reaction equation:



The maximum etched volume measured per cycle can be calculated by subtracting the etched volume for S_4 and S_5 . The resulting etched volume is found to be 0.2344 mm^3 . Given that the density and molecular mass of Si are 2.329 g/ cm^3 and 28.0855 g/mol, respectively, it can be determined that the number of actual etched Si moles in this reaction was 1.944×10^{-5} moles. This simple study reveals that the etching gas volume that had been injected into the chamber was sufficiently enough to etch at least more than double the etched Si volume and the reaction was absolutely time controlled. This is important to exclude any possibility of etchant gas limitation in the further comparisons.

Table 2 Loading details and associated etched volume according to the preferred recipe for one loaded sample

Sample Ref	S_1	S_2	S_3	S_4	S_5
no. of cycles	3	4	5	4	5
final diameter, μm	40	55	66	60	74
etched depth, μm	2.9	11.5	19.1	13	25.2
vertical/lateral ratio	2.9	1.369	1.369	1.2	1.389
etched volume, μm^3	0.012	0.093	0.214	0.12	0.354
etched volume per cycle	—	0.081	0.121	0.108	0.235

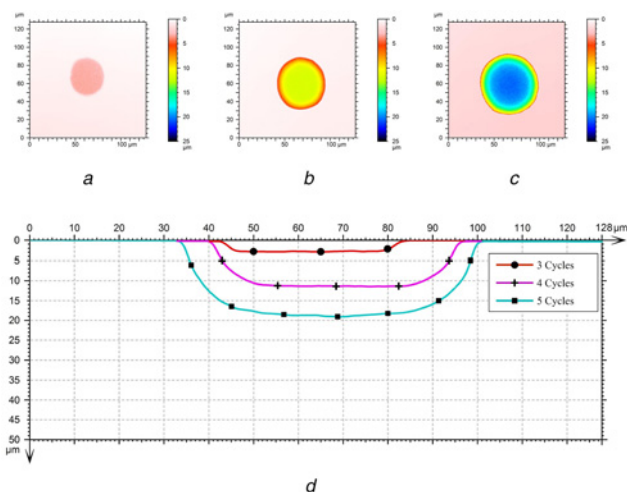


Fig. 6 Etching analysis showing the effect of increasing number of cycles
a 3 cycles,
b 4 cycles,
c 5 cycles,
d Surface profile comparison

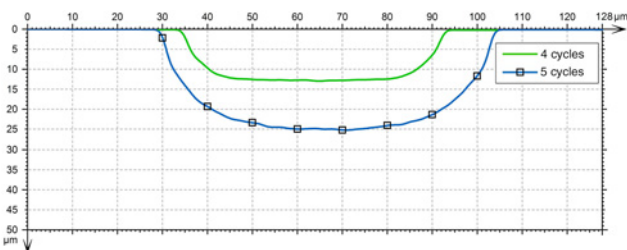


Fig. 7 Surface profile comparison after prolonged storage under vacuum for the cases of 4 and 5 cycles

The dependency on the number of cycles is summarised for three samples (S_1 , S_2 and S_3), which were introduced one by one for etching using 3, 4, and 5 cycles, respectively. Fig. 6 shows the coloured etching level as well as surface profile analysis for these three samples using ZEISS Confocal laser 3D microscope. The poor etching is very obvious at the early cycles, due to possible moisture and native oxide as pointed before, and the process takes a longer time to start and stabilise. Freshly prepared samples were thus required for etching to ensure the proper surface condition. Storing prepared samples under vacuum before etching preserves the surface from contaminants and can cause further surface condition enhancement, such as moisture adsorption from the surface, and thus enhances the etching rate. The surface profile measurement of two samples (S_4 and S_5), that had been stored under vacuum for 72 h before being introduced into etching, is illustrated in Fig. 7. This measurement shows a slight higher etching rate compared to those presented in Fig. 6.

6. Conclusion: The microparabolic reflector has been fabricated throughout this work, to be integrated with nanoantenna coupled IR detector, and the micromachining process is highlighted. The XeF_2 etching technique has been selected for its well-known gentle near isotropic etching, high selectivity, fast throughput and low cost while maintaining the CMOS compatibility.

Since this process is dramatically dependent on the load, the detailed analysis for this process has been presented here providing the required recipe for the etching profile of interest in particular, according to the introduced load through the designed patterned samples. Through many samples that had been then introduced

into the etching process with different conditions as well as different etching parameters, the optimum etching parameters according to the proposed design had been defined as 5 cycles of 30 s at a gas input pressure of 3 Torr. The used pattern, in this case, was mainly a circular windows pattern of a $38\ \mu\text{m}$ in diameter in addition to few required alignment marks, which all together provided an initial total area of $3.7122\ \text{mm}^2$. Accordingly, the approximated etched volume was determined to be in the order $0.354\ \text{mm}^3$.

The analysis presented here does not take into account the effect of extra load due to the backside of the sample. For a precise process characterisation, however, the backside loading effect has to be minimised. It is thus recommended to mask the backside of the sample in the future work. The tendency for isotropic etching had been noticed to vary according to the aspect ratio of the pattern. For the analysed samples, this dependency hinders the formation of the parabolic reflector to a depth of $>10\ \mu\text{m}$ below the sample surface level. Using a thicker mask is thus expected to provide the reflector formation much closer to the surface and thus reducing the difficulties of the cavity filling flatness in the subsequent process.

7 References

- [1] Grover S., Dmitriyeva O., Estes M.J., *ET AL.*: 'Traveling wave metal-insulator-metal diodes for improved infrared bandwidth and efficiency of antenna coupled rectifiers', *IEEE Trans. Nanotechnol.*, 2010, **9**, (6), pp. 716–722
- [2] González F.J., Boreman G.D.: 'Comparison of dipole, bowtie, spiral and log-periodic IR antennas', *Infrared Phys. Technol.*, 2005, **46**, pp. 418–428
- [3] Donchev E., Pang J.S., Gammon P.M., *ET AL.*: 'The rectenna device: from theory to practice', *MRS Energy Sustain. A Rev. J.*, 2014, **1**, p. E1
- [4] Novotny L., Van Hulst N.: 'Antennas for light', *Nat. Photon.*, 2011, **5**, (2), pp. 83–90
- [5] AbdelRahman M., Kusuma A.: 'Reception efficiency, resonant lengths and resonant input resistances of an infrared dipole antenna', *Optoelectron. Adv. Mater. Rapid Commun.*, 2010, **4**, (3), pp. 369–372
- [6] Florence L.A., Slovick B.A., Kinzel E.C., *ET AL.*: 'Infrared linear tapered slot antenna', *IEEE Antenna Wirel. Propag. Lett.*, 2011, **10**, pp. 1299–1301
- [7] Fumeaux C., Gritz M.A., Codreanu I., *ET AL.*: 'Measurement of the resonant lengths of infrared dipole antennas', *Infrared Phys. Technol.*, 2000, **41**, pp. 271–281
- [8] Shelton D.J., Sun T., Ginn J.C., *ET AL.*: 'Relaxation time effects on dynamic conductivity of alloyed metallic thin films in the infrared band', *J. Appl. Phys.*, 2008, **104**, (10), p. 103514
- [9] Middlebrook C.T., Krenz P.M., Lail B.A., *ET AL.*: 'Infrared phased-array antenna', *Microw. Opt. Technol. Lett.*, 2008, **50**, (3), pp. 719–723
- [10] Bean J.A., Weeks A., Boreman G.D.: 'Performance optimization of antenna-coupled Al/AlOx/Pt tunnel diode infrared detectors', *IEEE J. Quantum Electron.*, 2011, **47**, (1), pp. 126–135
- [11] Fumeaux C., Herrmann W., Kneubühl F., *ET AL.*: 'Nanometer thin-film Ni-NiO-Ni diodes for detection and mixing of 30 THz radiation', *Infrared Phys. Technol.*, 1998, **39**, (3), pp. 123–183
- [12] Bean J.A., Tiwari B., Szakmány G., *ET AL.*: 'Long wave infrared detection using dipole antenna-coupled metal-oxide-metal diodes', 33rd International Conference on Infrared, Millimeter and Terahertz Waves, CA, USA, 2008, pp. 1–2
- [13] Krenz P.M., Tiwari B., Szakmany G.P., *ET AL.*: 'Response increase of IR antenna coupled thermocouple using impedance matching', *IEEE J. Quantum Electron.*, 2012, **48**, (5), pp. 659–664
- [14] Mubarak M., Sidek O., Abdel-Rahman M., *ET AL.*: 'Spherical reflector backed structure to enhance dipole antenna coupled IR detector performance'. 2014 IEEE Asia-Pacific Conf. on Applied Electromagnetics (APACE), Johor Baru, Malaysia, 2014, pp. 220–223
- [15] Mubarak M.H., Sidek O., Abdel-Rahman M.R., *ET AL.*: 'Surface wave loss reduction by spherical reflector enhances antenna coupled IR detector performance'. 2015 IEEE Int. RF and Microwave Conf. (RFM), Sarawak, Malaysia, 2015, pp. 268–271

- [16] Xuan G., Adam T.N., Suehle J., *ET AL.*: 'Xenon difluoride dry etching of Si, SiGe alloy and Ge'. 2006 Int. SiGe Technology and Device Meeting, NJ, USA, 2006, pp. 1–2
- [17] Hajj-Hassan M., Cheung M., Chodavarapu V.: 'Dry etch fabrication of porous silicon using xenon difluoride', *Micro Nano Lett. IET*, 2010, **5**, pp. 63–69
- [18] Chu P.B., Chen J.T., Yeh R., *ET AL.*: 'Controlled pulse-etching with xenon difluoride'. 1997 Int. Conf. on Solid State Sensors and Actuators – TRANSDUCERS '97, Chicago, USA, June 1997, vol. 1, pp. 665–668
- [19] Chan I.W.T., Brown K.B., Lawson R.P.W., *ET AL.*: 'Gas phase pulse etching of silicon for MEMS with xenon difluoride'. Engineering Solutions for the Next Millennium. 1999 IEEE Canadian Conf. on Electrical and Computer Engineering (Cat. No.99TH8411), Edmonton, Canada, 1999, vol. 3, pp. 1637–1642
- [20] Galijatovic A., Darcy A., Acree B., *ET AL.*: 'Molecular dynamics simulations of reactions of hyperthermal fluorine atoms with fluorosilyl adsorbates on the Si {100}-(2 × 1) surface', *J. Phys. Chem.*, 1996, **100**, (22), pp. 9471–9479
- [21] Hefty R.C., Holt J.R., Tate M.R., *ET AL.*: 'Mechanism and dynamics of the reaction of XeF₂ with fluorinated Si(100): possible role of gas phase dissociation of a surface reaction product in plasmaless etching', *J. Chem. Phys.*, 2009, **130**, (16), p. 164714
- [22] Veyan J.-F., Halls M., Rangan S., *ET AL.*: 'XeF₂ induced removal of SiO₂ near Si surfaces at 300 K: an unexpected proximity effect', *J. Appl. Phys.*, 2010, **108**, (11), p. 114914
- [23] Williams K.R., Gupta K., Wasilik M.: 'Etch rates for micromachining processing – part ii', *J. Microelectromech. Syst.*, 2003, **12**, (6), pp. 761–778
- [24] Su K., Tabata O.: 'Effects of aperture size and pressure on XeF₂ etching of silicon', *Microsyst. Technol.*, 2002, **9**, (1), pp. 11–16
- [25] Sarkar D., Baboly M., Elahi M., *ET AL.*: 'Determination of etching parameters for pulsed XeF₂ etching of silicon using chamber pressure data', *J. Micromech. Microeng.*, 2018, **28**, (4), p. 045007
- [26] Floarea G., Packirisamy M., Stiharu I.: 'Modelling and verification of XeF₂ silicon micromachining', *Int. J. Nanomanuf.*, 2009, **3**, (1–2), pp. 55–72
- [27] Easter C., O'Neal C.B.: 'Characterization of high-pressure XeF₂ vapor-phase silicon etching for MEMS processing', *J. Microelectromech. Syst.*, 2009, **18**, (5), pp. 1054–1061
- [28] Folks W.R., Ginn J., Shelton D., *ET AL.*: 'Spectroscopic ellipsometry of materials for infrared micro-device fabrication', *Phys. Status Solidi (C)*, 2008, **5**, (5), pp. 1113–1116
- [29] Huang Y., Boyle K.: 'Antennas: from theory to practice' (John Wiley & Sons, Inc., 2008)
- [30] González F.J.: 'Antenna-coupled infrared focal plane array'. PhD thesis, 2003